

5. Electron Spectra from Condensed Matter

5.1 Introduction

Electron spectra produced within a solid target irradiated by fast charged particles differ in many respects from spectra obtained from a gas target. Unfortunately, it is very difficult to measure directly the spectrum of internal electrons produced in the solid so this has been done only for a few limited cases. Generally, the spectra of electrons are recorded outside the solid, and they are modified by interactions during migration to the surface as well as by the transmission through the surface. Additional electrons produced in these interactions are included in the observed spectra (Figure 5.1).

To analyze the process of secondary electron emission from solids, the sequence of events is divided into three stages: 1) production of internal secondaries as a result of the interaction between the primary (incident) particle and the target electrons and atoms, 2) the migration of the liberated electrons to the surface, and 3) their escape through the surface into vacuum. These three stages are shown schematically in Figure 5.1. This is a simplified picture since the secondary electron is shown as continuing its motion through the solid along a straight line without any further collisions, and the incident particle makes only a single collision. In the case of incident electrons, it is not possible to distinguish between secondaries or primaries in the spectra obtained outside the solid. A large fraction of the electrons in the spectra are primary electrons which have been deflected or slowed down inside the target. Generally, a reflected or transmitted electron undergoes so many collisions that it is impossible to distinguish between stages 1 and 2.

A typical external spectrum resulting from electron bombardment of solids is displayed in Figure 5.2. Since it is not possible to distinguish between secondary electrons and primary electrons that have been slowed down, it is customary to divide the emitted electrons into two groups: those with energies less than 50 eV which are taken to be the true secondaries and those between 50 eV and the primary energy E which are the reflected (backscattered) electrons. The total yield of electrons with energies up to 50 eV is called δ and that of the reflected electrons η . Of course, this arbitrary division does not reflect the origin of a particular electron, but it is convenient since the behavior of slow electrons in solids differs from that of electrons with energies above 50 eV. In contrast, for ion-induced electron emission *all* electrons are secondary particles. This fact makes the interpretation of ion-induced electron spectra simpler than electron-induced spectra.

The rapid development of ultrahigh vacuum (UHV) technique during the last twenty years has stimulated a renewed activity in studies of secondary electron emission from solids since the number and the corresponding energy distribution of electrons with energies below 10 eV depend critically on the surface conditions. Generally, only results obtained from clean surfaces prepared by ion sputtering or in-situ film deposition can be considered as reliable for these low energies. With increasing exit energies, the requirements for the experimental procedure become less critical, and for the highest exit energies considered (1 to 3 MeV), the surface preparation hardly plays any role.

In many cases, one may utilize the similarity between electron spectra induced by electrons and those induced by fast protons. Stages 2) and 3) do not depend on the type of primary particle, and for electrons as well as protons of high speed, several theoretical treatments (see Sections 2.6, 2.7, and 2.8) predict that the cross section for ionization of the i 'th subshell depends essentially only on the speed of the primary particle. Unfortunately, experimental data comparing spectra from electron and proton impact on solids are scarce. Examples are the energy spectra from polycrystalline niobium obtained for 3-keV electron and 400-keV proton impact by Musket (1975) as shown in Figure 5.3. Even though the impact speeds are not the same, the spectra are indeed very similar. This similarity simplifies the discussion of external electron spectra at low ejection energies induced by electron bombardment, since there exists a large amount of high quality data on spectra obtained by fast protons.

5.2 Experimental Methods

The experimental methods that are applied to solid surfaces are, in many respects, similar to those for the gas phase. The angular resolved cross section is often measured with a spectrometer with the angle variable relative to the beam direction for backward as well as forward directions for thin film targets (Toburen, 1990; Combecher *et al.*, 1978; Folkmann *et al.*, 1975).

A typical experimental arrangement for measuring $d\delta/d\epsilon_1$ analogous to $\sigma(e)$ in gas phase experiments is shown in Figure 5.4. Such a spherical setup is only feasible for bulk solids or thin films, since the target density has to be sufficiently high. This apparatus was used by Hasselkamp (1985) and Hasselkamp *et al.* (1981) to make a comprehensive series of measurements of secondary electron yields and backward-ejected electron spectra. The chamber pressure was

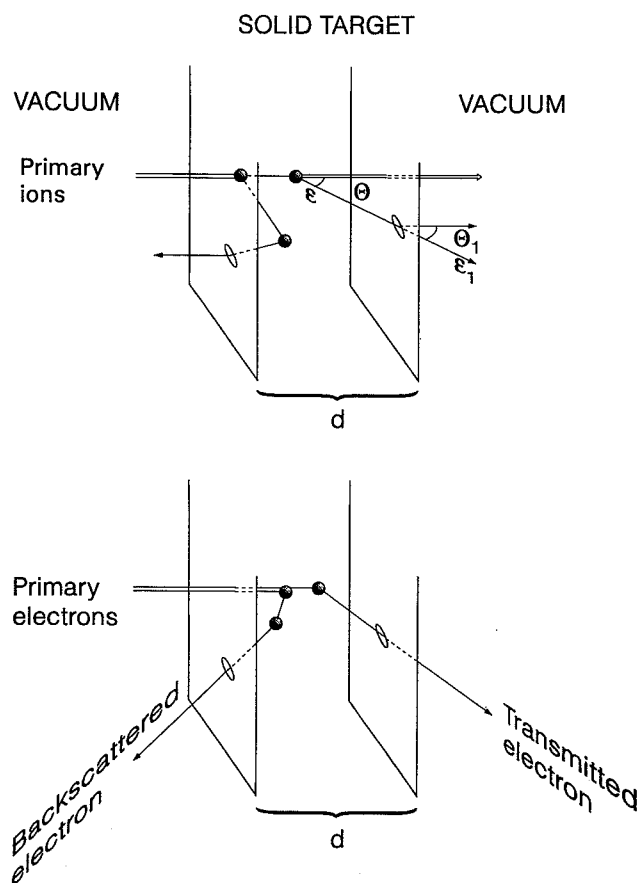


Fig. 5.1. Schematic view of the geometry for a particle penetrating a thin target of thickness d . "The upper figure shows a primary ion producing either a backscattered secondary electron or a forward scattered electron with energy ϵ inside the solid and energy ϵ_1 when it emerges from the solid. The lower figure shows the same for an incident electron. The ellipses indicate points on the surface where the electrons emerge from the solid."

below 4×10^{-9} torr and the surface of the target was cleaned by sputtering prior to each measurement. By applying a positive voltage to the target, the target-collector system could be operated as a concentric spherical analyzer in the retarding field mode. In this manner, the energy distribution of the emitted electrons induced by ion bombardment was determined for a variety of metals and for silicon (Hasselkamp, 1985; Hasselkamp *et al.*, 1987). The total secondary electron yields were measured with this apparatus as well.

The first results from foil experiments performed in UHV were reported by Rothard *et al.* (1990). These authors sputter-cleaned thin films with 800-keV Ar ions prior to the measurements. A typical result for ion bombardment is shown in Figure 5.5. The spectrum in the forward direction ($\theta = 0^\circ$) is similar to those obtained for gas-phase measurements and exhibits a low-energy peak and a pronounced peak of convoy electrons, *i.e.*, electrons with the same velocity as the projectile. This latter peak is absent at $\theta = 65^\circ$. Both peaks are sensitive to surface impurities. Roth-

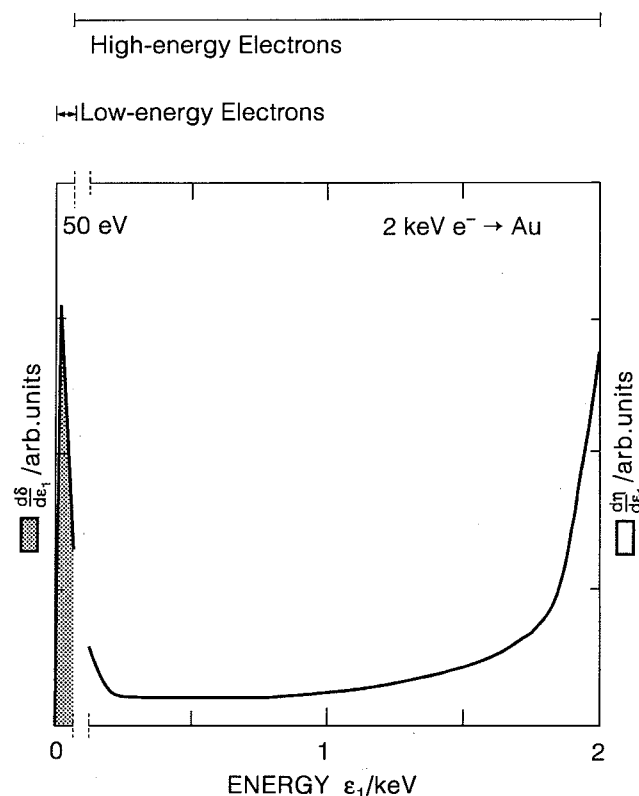


Fig. 5.2. Schematic spectrum of electrons backscattered from a solid for 2 keV electrons incident on gold. The hatched area corresponds to the secondary electron yield δ ; the white area to the reflection yield η (from Schou, 1994).

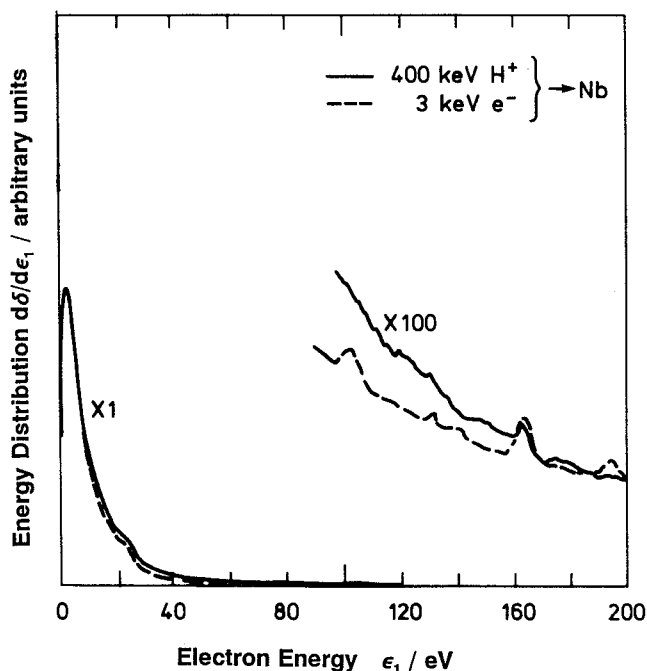


Fig. 5.3. Energy spectra of electrons ejected into the backward hemisphere from solid niobium under bombardment by electrons (angle of incidence not specified) and protons with the angle of incidence $\theta = 45^\circ$ under UHV conditions (from Musket, 1975). The energy distributions have been normalized at the peak maximum.

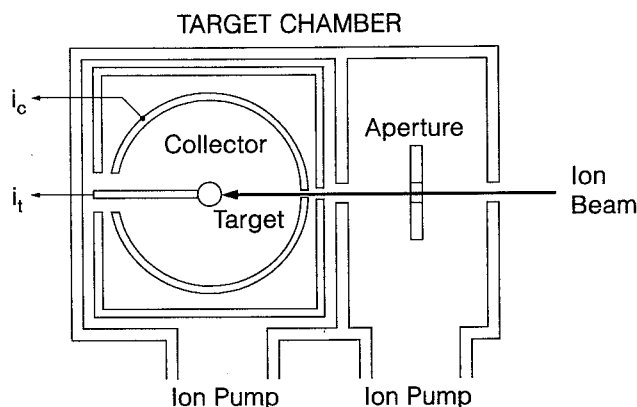


Fig. 5.4. Target chamber for measuring the electron spectrum emitted into the backward hemisphere and the secondary electron yield. i_t , target current; i_c , collected current (from Hasselkamp *et al.*, 1981).

ard and Burkhard (1988) found that the convoy electron yield increased with increasing residual surface coverage, whereas the yield of electrons from the low-energy peak is smaller for clean targets than contaminated ones (see Section 5.7).

5.3 Production of Free Internal Electrons

Differences between electron spectra from solids and gases occur at all stages of the electron emission process. The absorption of energy which eventually leads to free electron production depends strongly on the material (Inokuti, 1991). The atomic and molecular properties of materials characterized by weak

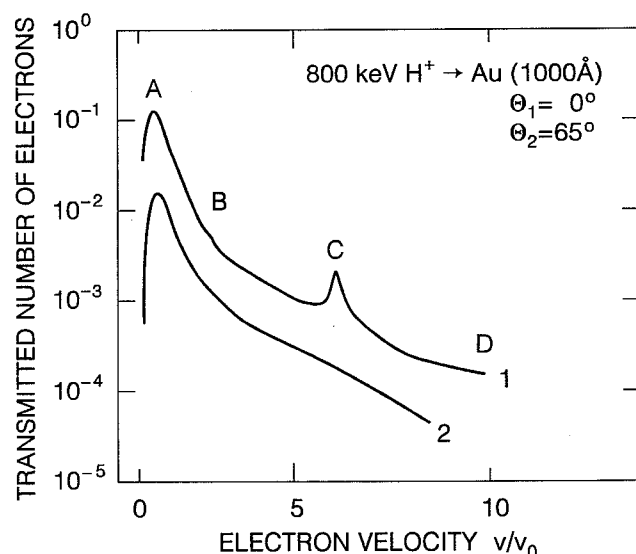


Fig. 5.5. Energy spectra (in arbitrary units) of electrons emitted at two angles in the forward direction with speed v in units of the Bohr speed v_0 from a sputter-cleaned Au foil of thickness 1000 Å under UHV conditions during bombardment by 800-keV protons at perpendicular incidence. A, low energy electron peak; B, Auger peak for Au; C, convoy peak; D, binary encounter shoulder (from Rothard *et al.*, 1990).

interatomic van der Waal's forces differ little between gas and solid. The photoabsorption cross sections for these materials in the solid phase is similar to those in the gas phase (Sonntag, 1977). Therefore, the production cross section for electrons in these solids should be similar to that in the gas phase. The reason is that the characteristic energies such as the ionization energy and dissociation energy for molecules are as much as two orders of magnitude or more larger than the cohesive energy in the solid. This is the case, *e.g.*, for solid argon, nitrogen and oxygen.

By contrast, the electronic levels of metal atoms are much different for free atoms and for the solid consisting of the same atoms (see Figure 5 of Bichsel, 1993). The outer shell electrons form the conduction band which consists of free electrons, whereas the more tightly bound electrons remain with the parent atoms. Consequently, the excitations are either delocalized single electron or resonant transitions of the free conduction electrons or localized ones of the deep levels of the atoms.

As an intermediate case, water, organic materials and other molecular solids exhibit largely localized excitations, but collective features have been observed (Isaacson, 1972; Inokuti, 1991).

5.3.1 Dielectric Response Theory

For metals, one may describe the interaction between the primary particle and the free electrons in a metal by a free-electron-gas model. The interactions between the incident particle and the electrons of the medium are treated on the basis of dielectric response theory (Lindhard, 1954; Landau and Lifshitz, 1960; Jackson, 1975; Fano, 1963). As a starting point consider the stopping power

$$\frac{dE}{dx} = -n \int d\epsilon \epsilon \sigma(\epsilon) \quad (5.1)$$

rather than the production cross section $\sigma(\epsilon)$. A uniformly moving particle with a point charge $Z_1 e$ and velocity \vec{v} is exposed to a medium-dependent force

$$\vec{F} = Z_1 e [\vec{\mathcal{E}}(\vec{r}, t) - \vec{\mathcal{E}}_{\text{vac}}(\vec{r}, t)], \quad (5.2)$$

where the electric field $\vec{\mathcal{E}}$ is taken at the particle position $\vec{r} = \vec{v}t$. The analysis of forces is most conveniently performed by a Fourier transform in terms of the wavevector k of the electric field. The field

$$\vec{\mathcal{E}}(\vec{r}, t) = \frac{-1}{(2\pi)^3} \int d\vec{k} \frac{iZ_1 e \vec{k}}{k^2 \epsilon^L} e^{i\vec{k} \cdot (\vec{r} - \vec{v}t)} \quad (5.3)$$

is then determined by the Fourier components of angular frequency $\omega = \vec{k} \cdot \vec{v}$, in a medium characterized macroscopically by a dielectric constant ϵ^L (Sigmund, 1975). Hence, the resulting force is given by

$$\vec{F} = -\frac{iZ_1^2 e^2}{8\pi^3} \int d\vec{k} \frac{\vec{k}}{k^2} \left(\frac{1}{\epsilon^L} - \frac{1}{\epsilon_{\text{vac}}} \right). \quad (5.4)$$

where $\epsilon_{\text{vac}}^L = 8.854 \times 10^{-12} \text{ s}^2\text{C}^2\text{kg}^{-1}\text{m}^{-3}$ is the absolute vacuum permittivity. Since F must be directed opposite to \vec{v} and numerically equal to the stopping power, F must be real and

$$\frac{dE}{dx} = \frac{(Z_1 e)^2}{4\pi^2 \epsilon_{\text{vac}} U^2} \text{Im} \int_0^\infty \frac{dk}{k} \int_{-kv}^{kv} d\omega \omega \left(\frac{\epsilon_{\text{vac}}}{\epsilon^L} - 1 \right), \quad (5.5)$$

a result which was derived by Lindhard (1954) under more general assumptions. The result is based on perturbation theory in the sense that the reaction of the projectile on the field which it creates is neglected. Eq. 5.5 does not incorporate the rapid spatial variations of the field, but this shortcoming has been overcome by the introduction of a wavenumber-dependent dielectric constant $\epsilon^L(k, \omega)$.

Essentially, the complex dielectric constant,

$$\epsilon^L(k, \omega) = \epsilon_1^L(k, \omega) + i\epsilon_2^L(k, \omega), \quad (5.6)$$

enters into the stopping power via the quantity

$$\text{Im} \left[\frac{1}{\epsilon^L(k, \omega)} \right] = \frac{\epsilon_2^L(k, \omega)}{(\epsilon_1^L)^2 + (\epsilon_2^L)^2}. \quad (5.7)$$

This quantity represents the excitation cross section for the free-electron gas, which accounts roughly for the interaction between the primary and the conduction electrons. The integration in Eq. 5.5 has to be performed over a certain area in the ω - k plane which is equivalent to an integration with the dimensionless variables $y = \hbar\omega/E_F$ and $x = k/k_F$ where E_F is the Fermi energy and k_F the Fermi wavevector. The area, for which ϵ_2^L differs from zero, is limited by two parabolas and the x -axis (the hatched areas in Figure 5.6). This corresponds to the single excitation regime of free electrons. The other important contribution from Eq. 5.7 to the stopping power comes from the y_p curve for which ϵ_1^L and ϵ_2^L both are zero. This curve, which is determined by $\epsilon_2^L(k, \omega) = 0$, represents the collective excitations, the so-called plasmon contribution. At $k = 0$, $\omega = \omega_{\text{pl}}$, which is the well-known plasma frequency for an electron gas with a free-electron density n_e

$$\omega_{\text{pl}} = \sqrt{\frac{n_e e^2}{m_e \epsilon_{\text{vac}}^L}}. \quad (5.8)$$

For low electron or ion velocities, only single electron excitations are produced, since conservation of energy and momentum limits the area of integration. With increasing particle speed, the line integral contributes substantially as indicated in Figure 5.6. In the limit of high primary energy, the collective (plasmon) and single-electron excitations contribute equally to the stopping power (Lindhard and Winther, 1964).

The underlying excitation spectrum has been studied by a number of authors. Tung and Ritchie (1977) calculated the production spectrum for primary electrons of energy E for aluminum. The results shown in Figure 5.7 demonstrate that all spectra exhibit a

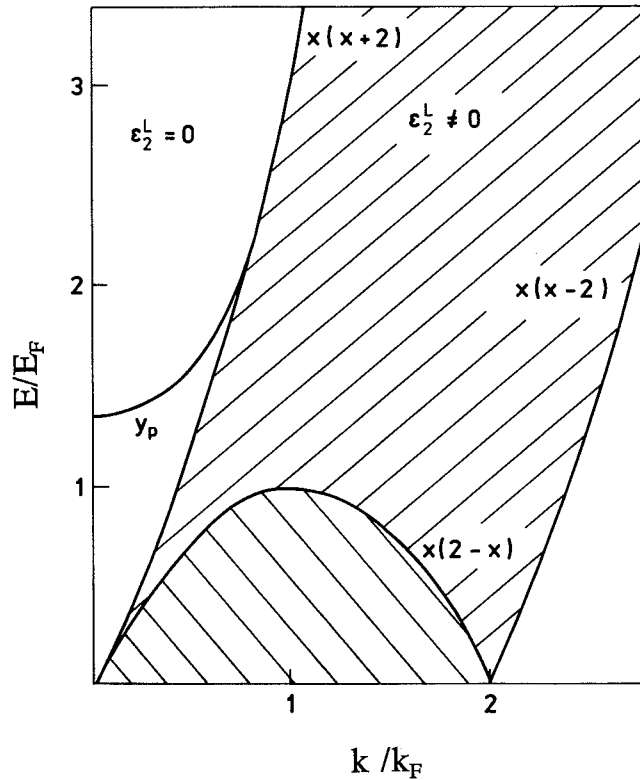


Fig. 5.6. Two-dimensional survey of the imaginary part ϵ_2 in the k - E plane for a free electron gas at the temperature $T = 0$. The dimensionless variables k/k_F and E/E_F are used. The hatched area indicates where $\epsilon_2^L \neq 0$. The two types of hatching represent two different analytical representations of ϵ_1^L . The solid curve shows the plasmon line y_p , for which ϵ_1^L and ϵ_2^L are both zero for a free-electron density corresponding to that of the conduction electron in aluminum.

maximum value around the energy $3E_F$ (measured from the bottom of the conduction band), where E_F is the Fermi energy, and falls off as ϵ^{-2} for high energy transfers corresponding to Rutherford scattering from electrons at rest. The peak around $3E_F$ is caused by the large values of the excitation cross section close to the plasmon curve shown in Figure 5.6. The production probability times the primary energy is described by the same curve except for the high-energy cut-off in the spectrum. Results for electron spectra have been obtained by Brice and Sigmund (1980) and Rösler and Brauer (1991). Brice and Sigmund (1980) derived the analytical approximation for producing an excited electron with an absolute wavevector k_1 :

$$d\sigma = \frac{Z_1^2 R a_0 k_1}{n_e m_e v v_F} dk_1 \cdot \left(\frac{1 - Z^*}{\alpha^2 + \chi^2} + \frac{Z^*}{\chi \alpha} \arctan \frac{Z^* - 1}{\frac{\chi}{\alpha} + \frac{\alpha Z^*}{\chi}} \right), \quad (5.9)$$

which is appropriate for the case $v \ll v_F$. Here $\alpha = (1 - \chi^2/3)^{1/2}$, $Z^* = (\epsilon - E_F)/2m_e v v_F$ and $\chi = 2R a_0/(\pi \hbar v_F)$. Results for projectiles with speeds v much greater than v_F were presented as well by these authors.

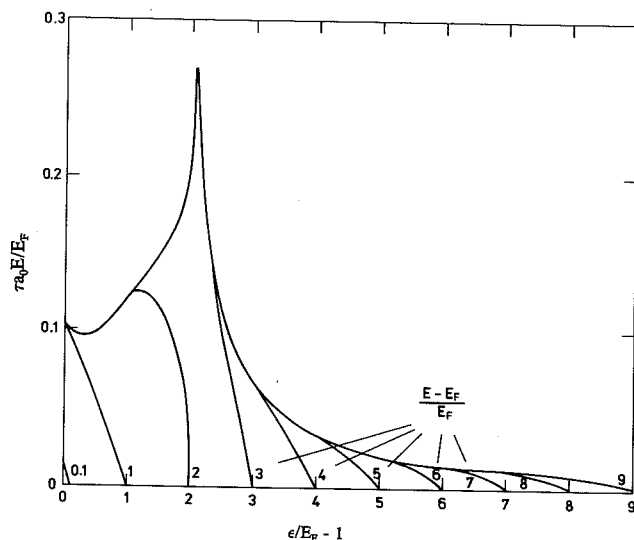


Fig. 5.7. Plot of the quantity $\tau_0 E/E_F$ vs. $\epsilon/E_F - 1$ where τ is the probability per unit length (the inverse mean free path) that an electron of energy E will create a secondary electron of energy ϵ in exciting electron-hole pairs in the electron gas (from Tung and Ritchie, 1977).

Tung and Ritchie (1977) calculated the differential inverse mean free path for creating a plasmon from an energy loss $\hbar\omega$ by a primary electron with energy E . Rösler and Brauer (1991) evaluated the plasmon formation and subsequent electron excitation from plasmon decay. These authors included plasmon damping beyond the free-electron model. The production spectrum for electron excitation is shown in Figure 5.8. For electron impact, the total contribution from plasmon decay decreases from 1 to 2 keV, whereas the shapes of the spectra are similar. For incident protons, the electron production has a maximum around 60 keV. The position of the maximum is determined by the increasing contribution from the line integral and the over-all decreasing one from the plasmon production as a function of projectile energy. The distribution of energy from plasmon decay has a tail up to considerably higher energies for proton impact than that for primary electrons.

The dielectric treatment has been utilized also in theoretical studies and Monte Carlo calculations of different aspects of electron emission from solids (Ganachaud and Cailler, 1979a; 1979b; Cailler and Ganachaud, 1990; Bichsel, 1990b; Devooght *et al.*, 1987; Dubus *et al.*, 1993).

5.3.2 Binary Encounter Theory

An alternative approach for electron collisions based on a binary encounter treatment for predicting internal spectra was originally made by Gryzinski (1965) and later improved by Shimizu and co-workers (Shimizu and Ichimura, 1983). The production spectra for an electron from the i 'th subshell with the

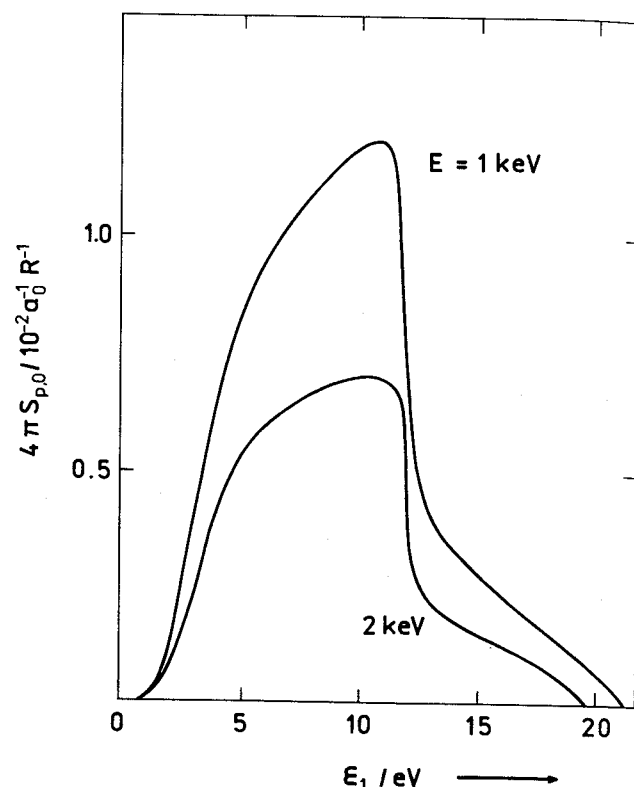


Fig. 5.8. Electron spectra produced by plasmon decay for 1- and 2-keV electrons. The excitation quantity $S_{p,0}$ in units of $0.01 R\alpha_0$ vs. the energy above the vacuum level $\epsilon_1 = \epsilon - U_B$ (from Rösler and Brauer, 1991).

binding energy B_i is given by

$$\sigma_i(\epsilon) = \frac{4\pi\alpha_0^2 R^2 B_i}{\epsilon^3 E} \left(\frac{E}{E + B_i} \right)^{3/2} \left(1 - \frac{\epsilon}{E} \right)^{B_i/(B_i + \epsilon)} \times \left\{ \frac{\epsilon}{B_i} \left(1 - \frac{B_i}{E} \right) + \frac{4}{3} \ln \left[2.7 + \left(\frac{E - \epsilon}{B_i} \right)^{1/2} \right] \right\}. \quad (5.10)$$

The full ionization cross section requires a summation over all subshells of the atom. Since this result is based on a classical treatment, it does not include any plasmon contribution. Therefore, the expression has been used primarily for solids with bound electrons or for the inner-shells in metal atoms. The binding energy of each shell is often treated as an adjustable parameter, which has led to an acceptable agreement for the integrated quantities such as the stopping power. In any case, the minimum requirement for consistency of these cross sections is that the corresponding integration of the production spectra gives the correct stopping power at high primary energies, *i.e.*, Bethe's stopping power (see *e.g.*, Shimizu and Ichimura, 1983; Valkealahti *et al.*, 1988; Cailler and Ganachaud, 1990; Schou, 1994). Valkealahti *et al.* (1989) used a cut-off at a certain energy as an adjustment to the stopping power, and this procedure could be performed for conduction electrons as well with some success (See Section 5.8). However, these

authors were primarily studying spatial deposition profiles of the kinetic energy of the slow electrons.

5.3.3 Charge-State Effects

A complicating feature for electron emission from solids induced by ions is the variety of charge states of the projectile that influence the secondary electron yield and the spectrum of secondaries. As soon as a beam of neutrals or charged ions penetrates into the solid, the average charge state changes toward the equilibrium charge state, which is determined by the instantaneous ion energy (Sigmund, 1975; Baragiola *et al.*, 1976; Betz *et al.*, 1988; Rothard, 1995). This charge equilibrium distance may exceed several tens of nanometers. The yield increases gradually with film thickness until the electrons liberated deep below the surface do not reach the backward or forward surface. Since the typical escape depth for electrons is often less than the equilibrium distance for all materials except a few insulators, the internal secondaries that are eventually ejected are produced by ions which have not yet reached the equilibrium charge state. An example of the secondary electron yield from the backward side of a carbon foil is shown in Figure 5.9 (Koschar *et al.*, 1989). The yield increases gradually with film thickness until the liberated electrons fail to reach the surface. The different branches pertinent to each charge state do not merge into one common curve, indicating that charge equilibration has not yet taken place. Similarly, the absolute magnitude of the electron spectra depends strongly on the charge state in the production process (see Section 4 and Sections 5.9 and 5.10).

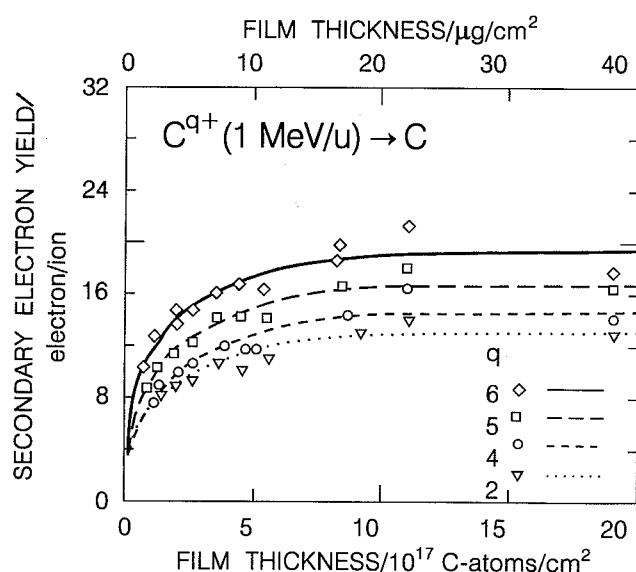


Fig. 5.9. Yield of secondary electrons with energies below 50 eV emitted from the back surface of carbon foils during the bombardment by C^{9+} with an energy of 12 MeV and $q=2-6$ as a function of target thickness (from Koschar *et al.*, 1989).

5.4 Migration of Liberated Electrons to the Surface

Electrons liberated by charged-particle interactions within a solid do not immediately escape from the point of production. Those with energies below 10 eV may be strongly scattered in collisions with core atoms or electrons or may even be absorbed in the solid. The behavior in the limit of low energies can be characterized as diffusion-like (Sigmund, 1993), but with increasing energy, the mean-free-path for collisions increases considerably. This means that the external energy ϵ_1 and angle θ_1 usually deviate from the values ϵ and θ for the internal production processes. However, for thin-film targets, one may obtain spectra that resemble those from gas phase targets. The results from Toburen (1990) (see Section 5.9) indicate that the absolute magnitude of angular resolved spectra agrees satisfactorily for electron energies above 30 eV, but apparently only in the forward direction. Even at these high energies, there are strong deviations around Auger-electron levels and above.

At low energies, the internal motion is primarily determined by the band structure of the solid. Electrons liberated in a metal will be slowed down as a result of the interactions with the conduction electrons. The collisions between the liberated electrons and the core atoms lead to strong scattering. The frequent scattering of the migrating electrons from the core atoms and the conduction electrons makes the internal distribution of electrons isotropic (Schou, 1980; Sigmund and Tougaard, 1981; Rösler and Brauer, 1991).

Knowledge of the low-energy stopping power for electrons is somewhat fragmentary (ICRU, 1984). For nearly-free-electron metals, one can apply the calculations by Tung *et al.* (1979) and Ashley *et al.* (1979) based on dielectric theory for a free-electron gas. The dependence of the stopping power on the free electron density is shown in Schou (1988). For low energies relative to the Fermi-energy level, the stopping power at the energy ϵ_0 is proportional to $(\epsilon_0 - E_F)^{5/2}$ (Nieminen, 1988). For noble and transition metals, the low-energy stopping power has been evaluated by Tung *et al.* (1979) as well, but the overall accuracy is much more questionable than that for nearly-free-electron metals.

The scattering of slow electrons on core or neutral atoms in a solid has been treated by several authors. Even though the calculations have been performed almost exclusively for metals, the results give a general guideline. Because of quantum effects, the scattering has to be determined from the phase shift or similar methods (Ganachaud and Cailler, 1979a; 1979b; Shimizu and Ichimura, 1983; Valkealahti and Nieminen, 1984; Cailler and Ganachaud, 1990; De-

vooght *et al.*, 1991; Rösler and Brauer, 1991; Schou, 1994). At energies below 100 eV the mean-free-path for an elastic collision in aluminum is less than 0.5 nm. This means that practically all slow electrons that reach and leave the surface have undergone a series of collisions.

The slowing-down of electrons in insulators is primarily characterized by the energy threshold for electron-electron interaction. Typically, there is an energy gap of a few eV between the valence electron levels and the empty conduction bands and excitonic levels in the energy gap somewhat below the bottom of the conduction band. Electrons with energies much higher than the energy gap are slowed down essentially as an electron in a metal. However, at electron energies close to the energy gap, statistical fluctuations strongly influence the slowing-down spectrum of electrons (Inokuti, 1975 and Kimura, *et al.*, 1993). For electron energies below the lowest excitonic levels, the stopping originates from the elastic interaction with the atoms alone. Eventually, the electrons may reach a thermal equilibrium energy in the meV range above the bottom of the conduction band determined by the phonon modes of the material. However, in most of the molecular materials there is a high trapping probability for slow electrons.

Since the slowing-down of the electrons is fairly inefficient, insulating materials exhibit escape depths greater than several tens of nanometers for secondary electron emission (Schou, 1993). The stopping power for energies below the band gap has been evaluated in a few cases (Fano and Stephens, 1986; Knipp, 1988; Fano, 1988). At these low energies, the electron is delocalized over several atoms, so that the electron interacts simultaneously with many atoms. A typical slowing-down rate is 10 to 1000 meV/nm, but consistent, systematic computations do not exist (Nieminen, 1988). For molecular solids other processes, *e.g.*, trapping, are dominant.

The behavior of slow electrons in molecular solids is of particular interest because these solids often retain most of their individual atomic and molecular properties. This means that comparisons with gas-phase data are useful. The slow electron scattering processes may be described in terms of intermolecular resonant mechanisms and potential scattering (Sanche, 1990; 1991). With this approach, it has been possible to explain structures in the energy dependence of the inelastic collision cross section by the formation of transient negative ions.

The formation of anions is one of several capture or excitation processes which a slow excess electron may undergo (Sanche *et al.*, 1994). The electron may not only be attached to a neutral molecule but may also be solvated in a molecular solid. Usually, this single electron trapping involves an energetic adjustment of the surrounding electron clouds to a stable configuration of the trapped electron. These trapping and

polarization processes are typical for molecular solids and tend to limit the migration of mobile electrons:

5.5 Ejection from the Surface

With a few exceptions, all solids have a surface barrier that the electrons have to overcome during the ejection process. This is a typical effect for a condensed material. In metals, the height of the barrier U_B is determined by the Fermi-energy E_F and the work function Φ , whereas for insulators, the corresponding quantity is the electron affinity E_A , *i.e.*,

$$U_B(\text{metal}) = E_F + \Phi \quad (5.11)$$

and

$$U_B(\text{insulator}) = E_A. \quad (5.12)$$

Schematic views of the energy barriers for metals and insulators are shown in Figure 5.10. For clean metals, the work function varies between 4 and 6 eV except for the alkali metals which have lower values. The Fermi energy varies from about 1 eV for the heavy alkali metals to about 15 eV for aluminum and beryllium. For most insulators, E_A is slightly less than 1 eV (Bader *et al.*, 1984; Poole *et al.*, 1975).

Obviously, the surface barrier is so small that it only influences electrons of relatively low energy. The electrons are transmitted through the surface if the component of the kinetic energy associated with the component of velocity perpendicular to the surface exceeds the magnitude of the surface barrier:

$$\epsilon_1 \cos^2 \theta_1 = \epsilon_0 \cos^2 \theta_0 - U_B > 0, \quad (5.13)$$

where θ_1 and θ_0 are the angles the trajectory of the electron makes with the normal to the surface outside and inside the solid, respectively.

5.6 Primary Electrons: Low Energy Part of External Spectra

The purity of the surface mainly influences electrons with energies up to 10 eV. The spectrum from 10 eV to the arbitrary limit for low-energy electrons of 50 eV is essentially unaffected by the surface purity, but for energies below 10 eV only results from measurements performed in high vacuum with appro-

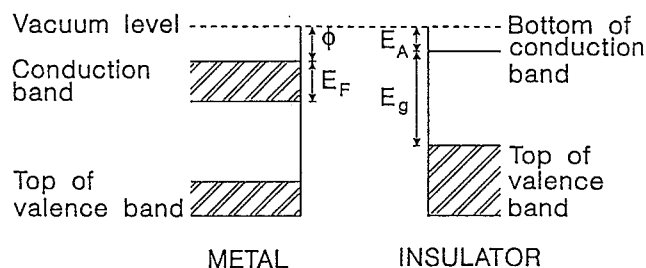


Fig. 5.10. Schematic view of the surface barrier for metals and insulators (from Schou, 1993).

appropriate cleaning procedures are useful. Results obtained during and after cleaning by ion-induced sputtering show how sensitive the absolute magnitude and shape of the spectrum are to impurities at the surface (Hasselkamp, 1985). One expects that a contaminated surface leads to an enhanced secondary electron yield as well as to a narrowing of the low-energy peak because contaminants are likely to be oxides or other insulators.

Figure 5.11 shows representative examples of external theoretical and experimental electron spectra from aluminum for primary energies around 1 keV (Schou, 1994). The experimental spectra have a most probable value in the range 1.5 to 1.9 eV, and fall off with increasing energy. The shape of the electron spectra reflects primarily the slowing-down of the internal secondaries by the electron-electron interaction and the surface barrier. The presence of a barrier results in an energy distribution which goes to zero with decreasing external energy ϵ_1 . The position of the peak maximum is, therefore, determined from one side by the magnitude of the barrier and from the other side by the energy loss rate of the migrating electrons.

An approximate guideline for the prediction of electron spectra is given in the theoretical treatments by Schou (1980) and Devooght *et al.* (1987). The internal flux that arrives at the surface is given by

$$\frac{d\delta}{d\epsilon_0} = \frac{c}{\epsilon_0 d\epsilon_0/dx}, \quad (5.14)$$

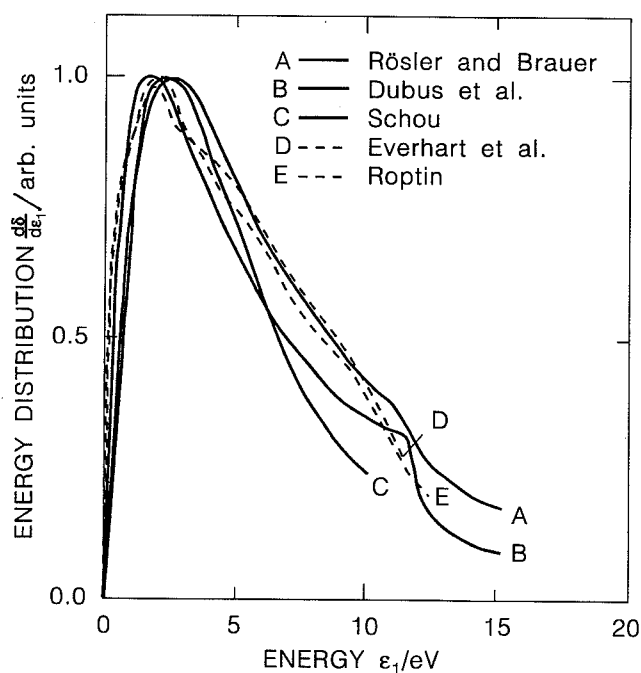


Fig. 5.11. The external energy distribution $d\delta/d\epsilon_1$ of electrons emitted backwards from an aluminum surface under UHV conditions during bombardment by electrons with an energy of about 1 keV. Theoretical curves, Rösler and Brauer (1991), Dubus *et al.* (1987) and Schou (1980). Experimental curves, $E=1$ keV, Everhart *et al.* (1976); $E=0.8$ keV, Roptin (1975).

where c is a constant that depends, for example, on the primary energy E . The quantity $d\epsilon_0/dx$ is the stopping power for low-energy electrons with kinetic energy ϵ_0 in the solid. Equation 5.14 is derived under the assumption that the low energy electrons are produced from cascade processes rather than by direct ionization by the primary particle. The emitted spectrum is modified by the surface barrier as given by

$$\frac{d\delta}{d\epsilon_1} = \frac{c_1 \epsilon_1}{\epsilon_0^2 d\epsilon_0/dx} \quad (5.15)$$

(Schou, 1988). A detailed prediction requires knowledge of the low-energy stopping power $d\epsilon_0/dx$ (see Section 5.4).

A comparison between the energy spectrum in Eq. 5.15 and the production spectrum in Figure 5.3 shows that both curves have a maximum and decrease as ϵ_0^{-2} for energies close to 50 eV (since the low-energy stopping power for aluminum is practically proportional to ϵ_0 between 20 and 50 eV). However, the peak in the production spectrum is much sharper than that from the external spectrum, and any similarity between the external spectrum and the production spectrum is accidental rather than fundamental.

Experimental spectra from well-characterized surfaces are available primarily for aluminum (Everhart *et al.*, 1976; Roptin, 1975; Bindi *et al.*, 1979). For silver surfaces, spectra have been measured by Bindi *et al.* (1979) and Roptin (1975), and for copper by Bindi *et al.* (1979). The results of Bindi *et al.* (1979) indicate that the most probable value is somewhat below Roptin's results and those obtained by proton bombardment from Hasselkamp *et al.* (1987).

A series of spectra measured by Roptin for aluminum shows that the shape is comparatively insensitive to variations of the primary energy. The position of the maximum varies very little from $E = 0.5$ to 1.5 keV, whereas the maximum shifts to a value twice as great as the energy is decreased from 500 to 100 eV. Even in this energy interval, no considerable change of the shape takes place. This tendency is supported by the theoretical treatments of Schou (1988) and of Devooght *et al.* (1987). In both cases, the expression for the energy distribution can be written as a function that depends only on material properties such as the low-energy electron stopping power and the surface barrier but not on the primary electron energy to a first approximation.

Jahrreiss and Oppel (1972) measured the angular distribution of the secondary electron coefficient from gold films. For perpendicular incidence, the angular distribution is virtually a cosine function in the forward as well as the backward direction.

An interesting feature is the contribution of electrons generated by volume plasmon decay in aluminum and magnesium. The shoulder shown at about 11 eV in Figure 5.11 originates from the decay of

plasmons. The contribution of surface plasmons to the spectra has recently been included in a Monte Carlo code by Cailler and Ganachaud (1990). The treatment by Rösler and Brauer (1988) demonstrates that the contribution to the spectrum from aluminum induced by 2-keV electrons is composed of almost equal parts from i) free electron excitation, ii) excitation of core electrons, and iii) decay of plasmons.

For primary electrons, a complicating aspect is the contribution of the backscattered electrons to the secondary electron spectra (Schou, 1988). The secondaries that are generated in the outermost layers by these backscattered electrons constitute a considerable fraction of the total yield. The reason is that the cross section for ionization or excitation is much larger for relatively slow backscattered electrons than for primaries in the keV range. The contribution from the backscattered electrons is generated by fast electrons at all energies between 50 eV and the primary energy E and in all backward directions. This feature is difficult to incorporate directly in a theoretical treatment. In Schou's treatment (1980) this problem has been solved by utilizing the known spatial distributions for deposited energy (Schou, 1988).

A number of additional theories have appeared in the literature (Bindi *et al.*, 1980; Dubus *et al.*, 1987; 1993). Many of them are based on transport equations from which the spectra and the yields have to be evaluated numerically. The dependence on the important physical parameters is, therefore, partly hidden. Monte Carlo calculations are available as well (Cailler and Ganachaud, 1990; Kotera *et al.*, 1990; Luo and Joy, 1990).

The starting point for any prediction of the magnitude or shape of an external electron spectrum should be an experimentally measured spectrum, if one exists. If no measurements are available, one may, as a good approximation for primary energies in the keV region, use spectra from proton bombardment. One may utilize the similarity of the spectra to obtain the approximate shape of the energy distribution at the primary energy desired. The absolute magnitude can be determined by integration over all exit energies, and the distribution may then be normalized to the secondary electron yield if it is known. If one wants to extrapolate the spectra to higher emission energies (< 50 eV), one may attempt to fit a spectrum to Eqs. 5.14 or 5.15. For transition and noble metals, one may use E_F as an adjustable parameter (see the next Section).

5.7 Light Ions: Low Energy Part of External Spectra

The status of knowledge of electron spectra from light-ion bombardment may be regarded as good. The majority of the spectra originate from the work by

Hasselkamp and coauthors. Spectra have been measured from many elements treated by sputter cleaning immediately before the bombardment by protons and light noble gas ions (Hasselkamp, 1985).

A number of spectra from proton-bombarded gold are shown in Figure 5.12 from Hasselkamp *et al.* (1987). One notes that the spectra are similar to those with incident electrons. There is a pronounced peak at a few eV originating from slow internal secondaries of first or higher generations. (Note that the peak is not seen in the figure.) With increasing energy the spectrum varies as ϵ_1^{-n} , where n lies between 1.5 and 2.

In contrast to electron bombardment, there is no contribution to the spectrum or to the secondary electron yield from backscattered primaries except at proton energies around or below a few keV. This simplifies the interpretation of the measured spectra considerably.

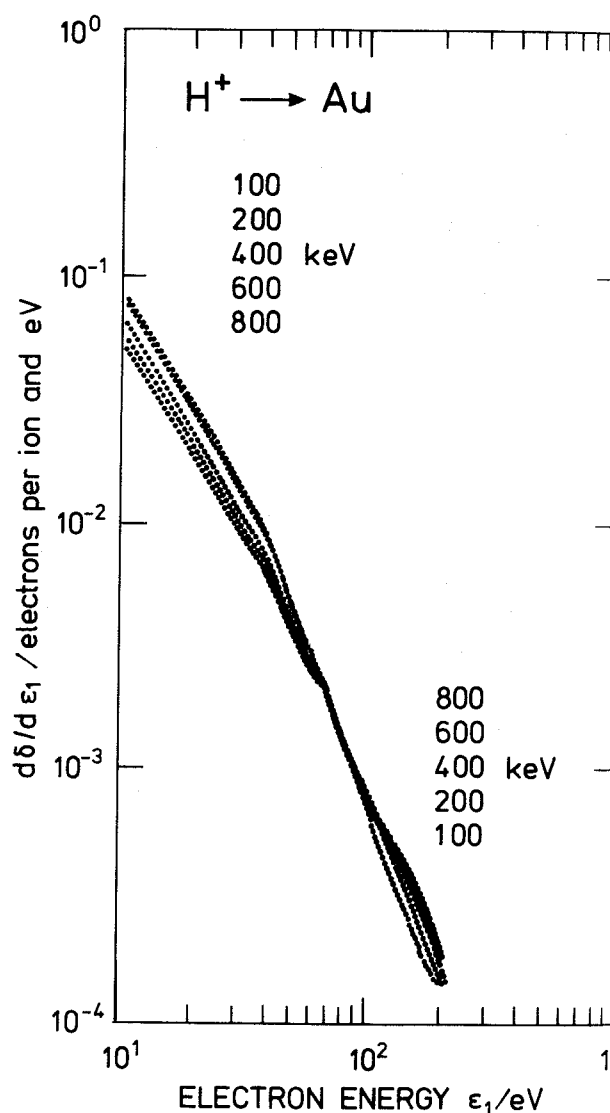


Fig. 5.12. External spectra of electrons emitted in the backward hemisphere from proton-bombarded gold under UHV conditions (from Hasselkamp *et al.*, 1987).

As for electron-induced spectra, the spectral distribution from protons is practically unchanged as the proton energy is varied from 70 to 800 keV. This similarity has been demonstrated by Hasselkamp (1985) and by Hasselkamp *et al.* (1987). The proton-induced yield has been measured by Hasselkamp (1985); he finds that the absolute magnitude depends on the primary energy as for spectra from electron bombardment.

The shape of the spectrum generally differs from one element to another. The position of the low-energy peak in the spectrum varies from 1.8 eV for silicon up to 3.6 eV for niobium, whereas the full width at half maximum varies from 6.0 eV for magnesium to 11.8 eV for titanium (Hasselkamp *et al.*, 1987).

Measurements by Drexler (1994) show that there are substantial deviations from a cosine distribution of electrons from proton-bombarded carbon foils. The foils were sputter-cleaned and the measurements performed under UHV conditions. The doubly differential electron yield for 0.5-MeV protons is shown in Figure 5.13. The curves are similar from 20 eV up to 200 eV except for the absolute magnitude. The spectra of electrons emitted in the backward direction follow a cosine distribution as a function of the exit angle (measured from the normal) for exit energies above 5 eV. Below 20 eV the spectra exhibit surprising differences and there seems to be a tendency for the position of the maximum of the low-energy electron yield to increase from a few eV to almost 10 eV with increasing ejection angle.

A direct prediction of the shape of the electron spectrum is given by Schou (1980). The energy distribution is given by Eq. 5.15, but the constant c_1 depends, as mentioned, on the material, primary energy and type of projectile. Using the low-energy electron stopping power from Tung *et al.* (1979),

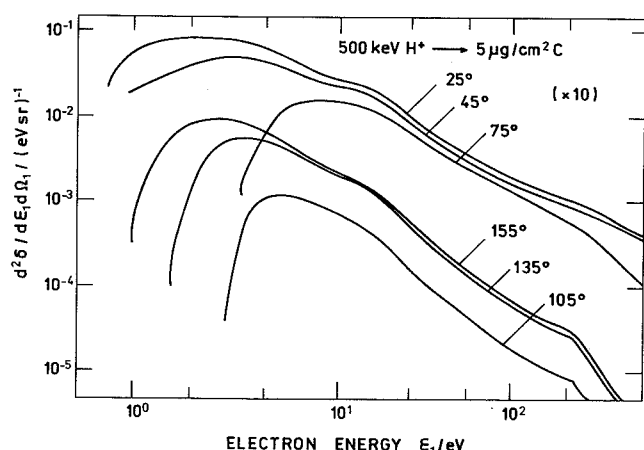


Fig. 5.13. Double differential spectra in the forward as well as the backward direction from a $5 \mu\text{g}/\text{cm}^2$ thick, sputter-cleaned carbon foil under UHV conditions bombarded by 500 keV protons at perpendicular incidence (from Drexler and Dubois, 1995).

Hasselkamp evaluated the theoretical spectrum for 400-keV protons incident on gold (Figure 5.14). It turned out that the choice for the magnitude of the surface barrier that led to the best agreement was $U_B = 14.1$ eV. The absolute magnitude of the theoretical curve was adjusted in such a way that the integral over the theoretical curve gave the experimentally determined yield. The agreement is satisfactory up to about 30 eV, but the theoretical curve underestimates the measured values considerably at higher energies. Since the low-energy electron stopping power for materials other than the nearly-free-electron metals are much less reliable, the estimate shown in Figure 5.14 demonstrates the present achievable accuracy of the theoretical prediction.

The energy distributions from the nearly-free-electron metals induced by ions show a shoulder that apparently originates from plasmon decay (Hasselkamp *et al.*, 1987). The position of the shoulder agrees well with the expected energy

$$\epsilon_1 = \hbar\omega_{\text{pl}} - \Phi, \quad (5.16)$$

where $\hbar\omega_{\text{pl}}$ is the plasmon energy, 15.7 eV for aluminum and 10.9 eV for magnesium. Until now, the plasmon contribution has been observed in the total energy distribution only for these two materials. No indications of plasmon decay was seen for beryllium, which has been comprehensively investigated by Hasselkamp (1985) as well.

The interpretation of the experimental data is strongly corroborated by the theoretical treatment by Rösler and Brauer (1991). Up to one-third of the total yield originates from plasmon decay at proton energies above 50 keV. For magnesium, Rösler's (1994)

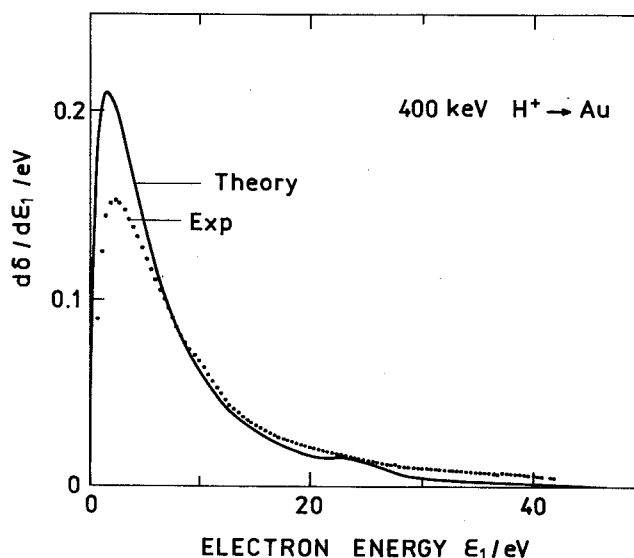


Fig. 5.14. Experimental external electron spectrum from gold induced by 400 keV protons (Fig. 5.12) and the corresponding theoretical spectrum, Eq. 5.15, from Schou (1980) with U_B adjusted to the best agreement ($U_B = 14.1$ eV), from Hasselkamp (1985).

treatment showed that the energy of the plasmon shoulder shifted to lower energies with increasing primary energy. This trend agrees with the data obtained by Hasselkamp (1985).

Generally, these features occur in the energy distribution only for nearly-free-electron metals. The reason is obviously that the electron density must not exhibit large variations throughout the volume occupied by the electrons, since the density determines the plasmon energy (Eq. 5.8). Noble and transition metals have a spatially varying density which leads to a smearing-out of the significant structures.

In energy spectra at a fixed exit angle, plasmon decay structures have been observed from thin carbon and copper foils as well (Burkhard *et al.*, 1988). However, the features were not visible without a sputter-cleaning procedure. In both cases, the structures were most pronounced at an angle of emission between 70° and 100° with respect to the forward direction.

5.8 Primary Electrons: High Energy Part of External Spectra

The available data cover the primary energy range from 1 keV to 3.3 MeV. Such a wide energy range requires experimental procedures which vary considerably throughout the interval. For energies below 5 keV the energy spectra (and the yield) of reflected electrons depend strongly on the purity of the surface. Consequently, a large amount of data obtained at low primary energies more than thirty years ago cannot be utilized, unless they agree satisfactorily with recent ones.

As a rule of thumb, the reflected electrons originate from depths up to one-half of the penetration depth in the solid. At the lowest energies (around 1 keV) the possible layers of contamination, therefore, play a relatively large role in the reflection of electrons. In contrast, at the high energies (around 1 MeV) the impurity layers constitute a very small fraction of the penetration depth, so that UHV conditions are less important.

The experimental results for 20-keV incident electrons by Matsukawa *et al.* (1974) shown in Figure 5.15 are an example of directly obtained external energy distributions. The spectra from the lighter elements differ considerably from those of heavier elements. For carbon, the spectrum is almost flat, whereas it peaks strongly close to the primary energy for gold. This means that there is a large contribution from the outermost layers in gold because of the large cross section for scattering for high atomic numbers (Ichimura and Shimizu, 1981), so that the scattered electrons have lost relatively little energy before ejection. For elements of low atomic numbers, there is a significant contribution to the number of re-

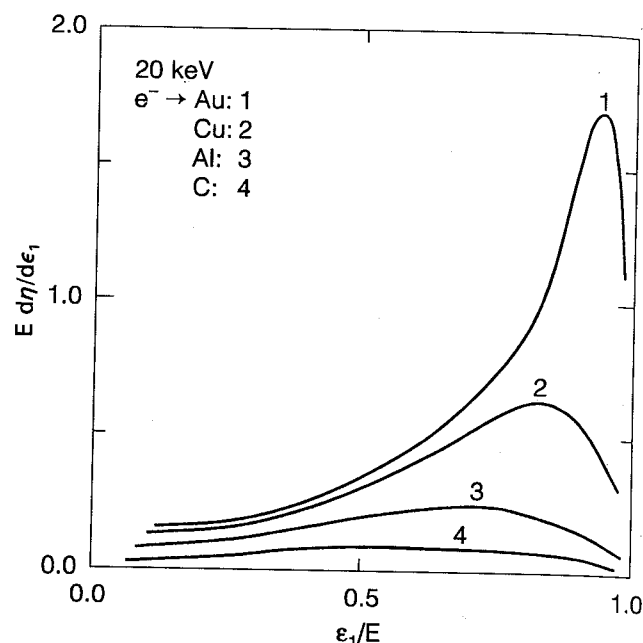


Fig. 5.15. External experimental spectra of electrons emitted into the backward hemisphere for four different metals during bombardment by 20-keV electrons at perpendicular incidence. The spectra are depicted in the scaled units, $E d\eta/d\epsilon_1$ vs. ϵ_1/E (from Matsukawa *et al.*, 1974).

flected electrons from large-angle scattering events. This leads to a flat spectrum, since the electrons may penetrate more deeply into the material before being backscattered, thereby losing more energy. In fact, this single scattering model (Everhart, 1960) could explain some features for energies below 10 keV and for light materials, but the reflection coefficient comes out a factor of two too small since multiple scattering is neglected.

The shape of the energy spectrum is characteristic of each element, but it varies only slightly with incident energy, as long as the spectrum is normalized to the primary energy E and the axes are in ϵ_1/E units. At higher energies, the peaks for materials of high atomic numbers move to lower energies (Matsukawa *et al.*, 1974).

The angular distribution of the yield of electrons, η , has been measured by Bronshtein *et al.* (1972) and Jahrreiss and Oppel (1972). Jahrreiss and Oppel found that the distribution may be well approximated with a cosine function for energies above 4 keV. Below this energy deviations from the cosine distribution occur predominantly for high Z_2 materials. Recently Massoumi *et al.* (1993) found a cosine distribution for 35-keV electrons as well.

An important series of measurements of electron spectra from a carbon foil was carried out by Combecher *et al.* (1978). These authors recorded angular-resolved electron spectra from two foils in the forward as well as the backward direction induced by 1-keV electron bombardment (Figure 5.16). Unfortu-

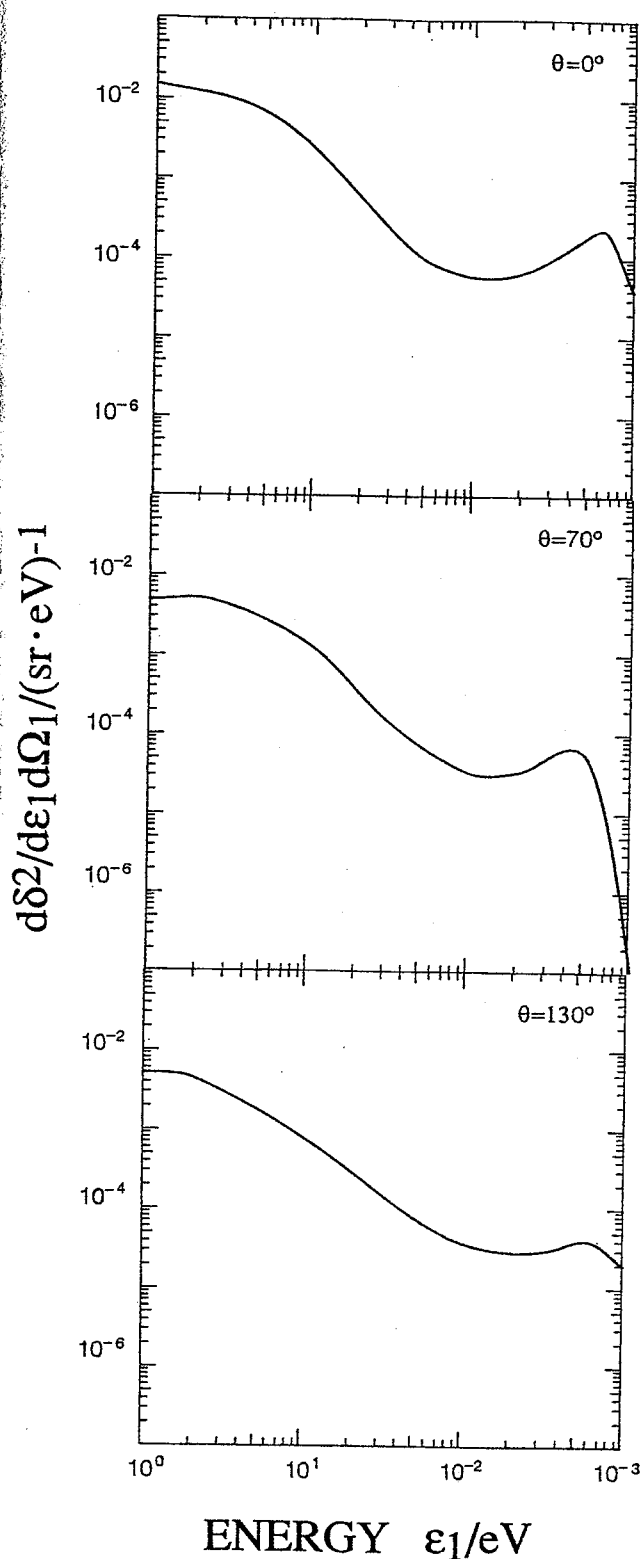


Fig. 5.16. External doubly differential energy spectra from thin carbon foils induced by 1-keV electrons (from Combecher *et al.*, 1978).

nately, the spectra were not obtained under UHV conditions, but the results are valuable because of the similarity between carbon foils and organic material. The precise thickness of the foils could not be deter-

mined, but the results match calculations for water foils of about 30 nm. The results obtained at low energies depend in any case on the surface contaminants which may be carbon as well. Above 50 eV the spectra are relatively flat except in the forward beam direction. In this direction, there is a pronounced minimum at around 300 eV and a peak close to 1 keV. These spectra were converted to internal distributions by the authors. Another important feature is that the angular distribution of the internal electrons appears to be practically isotropic.

There exist other data for the total external energy distribution between 10 and 70 keV. The spectra obtained by Kulenkampff and Spyra (1954) agree fairly well with those of Matsukawa *et al.* (1974). Darlington's spectra (1975) have been obtained by integration over spectra at specific scattering angles under several assumptions. The most probable value appears to lie too close to the primary energy compared to that from Matsukawa *et al.* (1974). The measurements by Kanter (1957) and Kulenkampff and Rüttiger (1954) for specific exit angles show essentially the same trends as those by Matsukawa *et al.* (1974).

Below 5 keV the experimental determination of the electron spectra becomes increasingly difficult. Even a small amount of impurities at the surface may change the shape of the distribution. Usually target contamination on heavy targets reduces the total number of reflected electrons as well, since impurities generally contain carbon atoms, which have a relatively low scattering cross section. The analysis must be based on results from Monte Carlo codes, which can be tested against experimental quantities that have been obtained for well-controlled surfaces.

A simulation of an external spectrum of reflected electrons from gold bombarded by 2-keV electrons at normal incidence is shown in Figure 5.17. There is a peak at very low energies which is due to the true secondary electrons and another at the incident energy which is due to scattered primaries. In this simulation, one can distinguish between true secondary electrons and primary electrons which have lost most of their energy in the collisions. Even though it is not experimentally possible to distinguish them, the figure shows that any calculation that does not include the generation of secondary electrons will have the wrong trend at low energies.

The code by Valkealahti and co-authors was developed for all elements and checked against results of reflection coefficients, thin-film transmission coefficients and spatial energy distribution curves, wherever these were available. The spectrum of Figure 5.17 was obtained with internal parameters that lead to convincing agreement with experimental data for the reflection coefficient for gold (Valkealahti *et al.*, 1988). The model was based on i) a modified Gryzin-

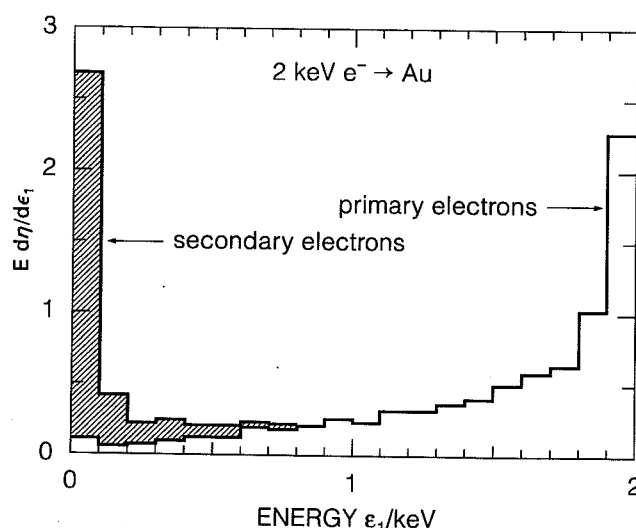


Fig. 5.17. Monte Carlo simulation of the external spectrum of electrons emitted in the backward hemisphere from gold induced by 2-keV electrons at perpendicular incidence. Hatched area, secondary electrons; white area, reflected electrons (from Valkealahti, 1987).

ski cross section for the electron-electron interaction and for the generation of secondaries, ii) a cross section for scattering on the core atoms derived from a partial wave expansion along the lines given by Ichimura and Shimizu (1981), and a cut-off for the bookkeeping of the electrons at 10 eV. It turned out that the code reproduced the experimental reflection coefficient only for a Gryzinski stopping power adjusted to the Bethe value at 10 keV (Valkealahti *et al.*, 1988). On the other hand, this adjustment meant that the stopping power agreed fairly well with that of Tung *et al.* (1979) down to a few hundred eV.

Figure 5.18 shows spectra for aluminum bombarded by 1.5- and 3-keV electrons from the Monte Carlo code developed by Shimizu and Ichimura (1983). From this figure one immediately recognizes the importance of the true secondaries as well. The peak close to the primary energy is less distinct for aluminum than for gold. The results from the code were tested against experimental $E d\eta/d\epsilon_1$ spectra and reflection coefficients from well-characterized aluminum surfaces. The code is based on i) a cross section for scattering on the core atoms from a partial-wave expansion, ii) Streitwolf's excitation function for conduction electrons (Streitwolf, 1959), iii) excitation cross sections for inner-shell electrons from Gryzinski's treatment, iv) energy loss to bulk plasmon generation according to Quinn's derivation (Quinn, 1962) and v) a cut-off for the bookkeeping at 100 eV. The total stopping power derived from these mechanisms is somewhat larger than that from Ashley *et al.* (1979), but the reflection coefficients from the code agree well with the experimental values. The computations by these authors confirm that the angular distribution of the reflected electrons is a cosine

function for perpendicular incidence of 1.5- and 3-keV electrons. At oblique angles of incidence there is a significant component of electrons scattered specularly. This Monte Carlo code was recently modified by Ding and Shimizu (1988) to include copper, silicon, and gold as well. These authors presented energy spectra from these materials induced by bombardment of 3-keV electrons. However, the total reflection coefficient, η , is considerably higher than those obtained experimentally.

An interesting feature is the strong no-loss peak which emerges from spectra for both primary energies. At the highest energies, the relative fraction of high-energy reflected electrons is enhanced.

At high electron energies, trends similar to those observed for elements of different atomic numbers by Matsukawa *et al.* (1974) are present in the spectra (Figure 5.19). These energy spectra from Rester and Derrickson (1970) have been obtained for 1-MeV electrons by integration of the data at various exit angles over the hemisphere. At even higher energies Frank (1959) has measured the energy distributions

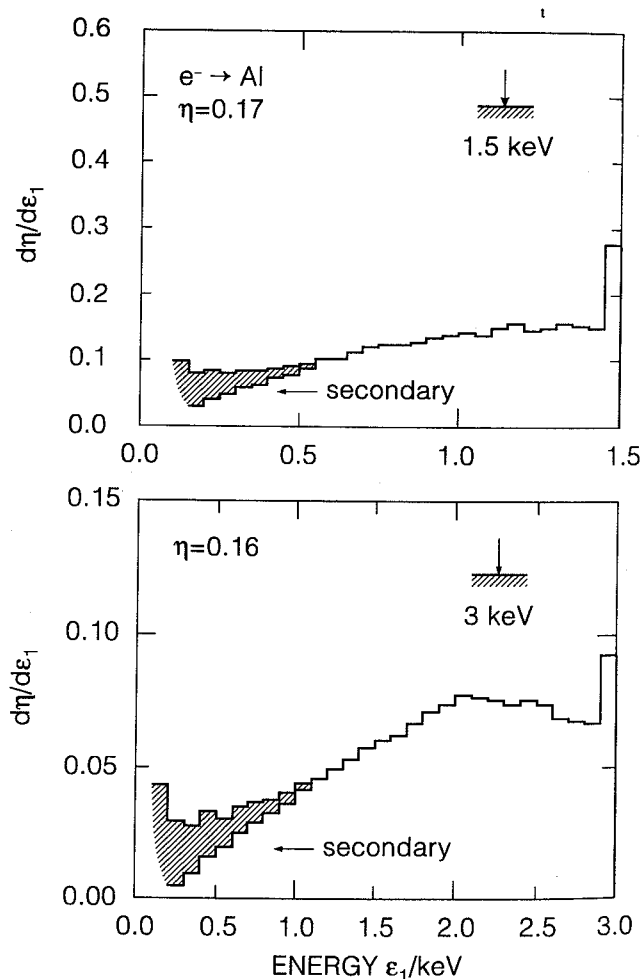


Fig. 5.18. Monte Carlo simulations of the electron spectra emitted in the backward hemisphere from aluminum induced by 1.5-keV and 3-keV electrons at perpendicular incidence (from Shimizu and Ichimura, 1983).

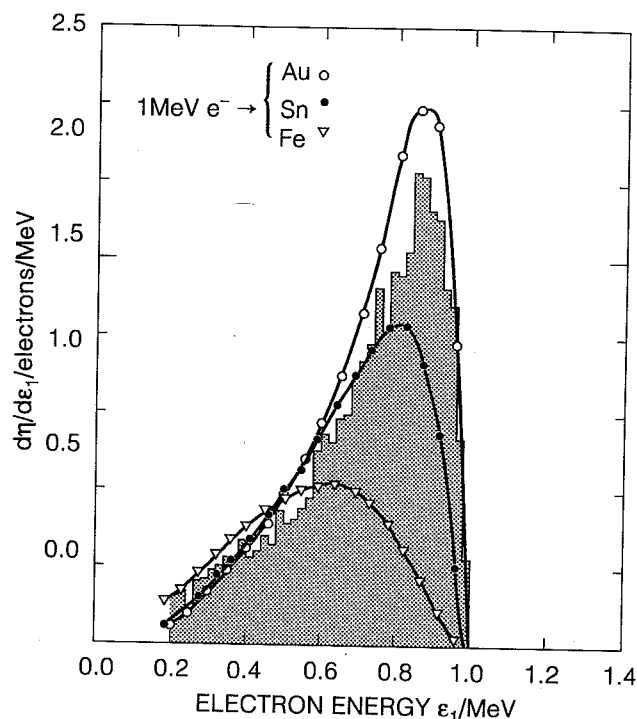


Fig. 5.19. External spectra of electrons emitted into the backward hemisphere from different metals induced by 1-MeV electrons at perpendicular incidence. The histogram for gold was calculated from the program ETRAN 15 by Berger and Seltzer (from Rester and Derrickson, 1970).

for a few exit angles for copper and lead. There is a considerable shift in the most probable energy to lower energies from 1.75 to 3.2 MeV (Figure 5.20). The shape of the distributions for different materials scales with Z_2/E (Frank, 1959; Harder, 1969).

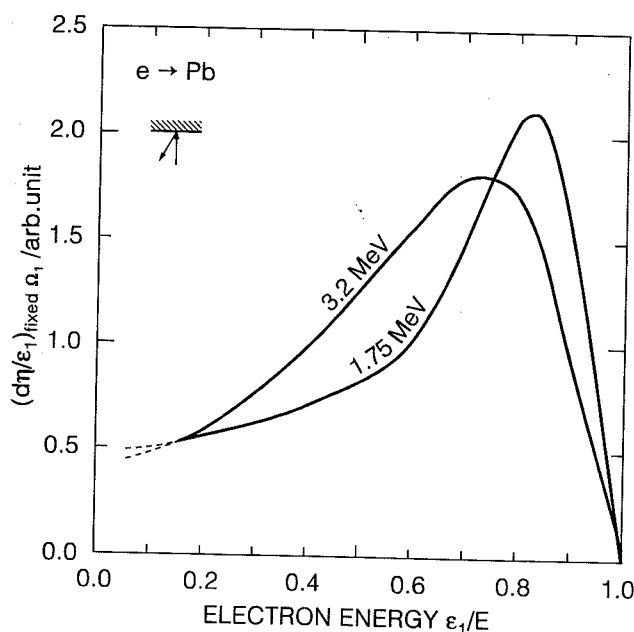


Fig. 5.20. Doubly differential spectrum for electrons ejected from lead at $\theta_1 = 150^\circ$ with respect to the beam direction induced by electrons at energies of 1.75- and 3.2-MeV at perpendicular incidence (from Frank, 1959).

The general tendency of the shape of the energy spectrum to change very little with primary energy is confirmed by Monte Carlo codes as well as theoretical studies. The important quantity is the ratio of the ejection energy ϵ_1 to the primary energy E . This is predicted by Tilinin's treatment (1982) as well. Secondary electron energy distributions for primary energies ranging from 1 keV up to several MeV may be calculated by scaling from the general shapes exhibited by the curves shown here. The scaling is done by plotting the cross section *vs.* ϵ_1/E .

5.9 Light Ions: High Energy Part of External Spectra

Several measurements of the high-energy part of the ion-induced electron spectra exist but most involve studies on foils in vacuums which were not sufficient to maintain clean surfaces. As discussed in Sections 5.2 and 5.5, the contaminants primarily influence the low-energy peak and to a certain degree the convoy peak (Figure 5.5). The only existing example of cross sections measured for the gas phase as well as two carbon foils in the same apparatus is shown in Figure 5.21. Unfortunately, the measurements were not carried out under UHV conditions. Nevertheless, the results indicate that the angular and energy spectra for the gas phase and the foils are fairly similar. Since the curves show the cross section per electron in the gas or foil target, the cross sections are directly comparable. Most of the liberated slow electrons are absorbed in the thickest foil and both sets of foil data tend to merge with the gas spectra as the exit energy increases. Higher-energy electrons have a greater range, and therefore, a greater probability of leaving the solid than slower ones. The characteristic Auger peaks are less pronounced in the foil than in the gas results. At energies above the Auger peak the cross section for ejection of electrons is greater than that for the gas. The reason is that high-energy electrons originally produced within the foil can be scattered and detected in the spectra at larger angles.

Measurements by Folkmann *et al.* (1975) of the energy spectra of electrons exiting from a carbon foil at a fixed angle of 42.3° with respect to the beam direction show features similar to those observed by Toburen (1990) and Rothard *et al.* (1990). Folkmann *et al.* irradiated the carbon foil with 0.5-MeV/u H^+ and Ne^{+2} ions but the data were not obtained under UHV conditions. Toburen (1990) has pointed out that the curves for these two ions could be normalized to each other at 800 eV. This normalization is consistent with the finding of the authors that the integrated energy distribution scales with the square of the net charge q of the primary ion. The yield for low exit energies, for which distant collisions are dominant, is higher for protons. The screening of the projectile

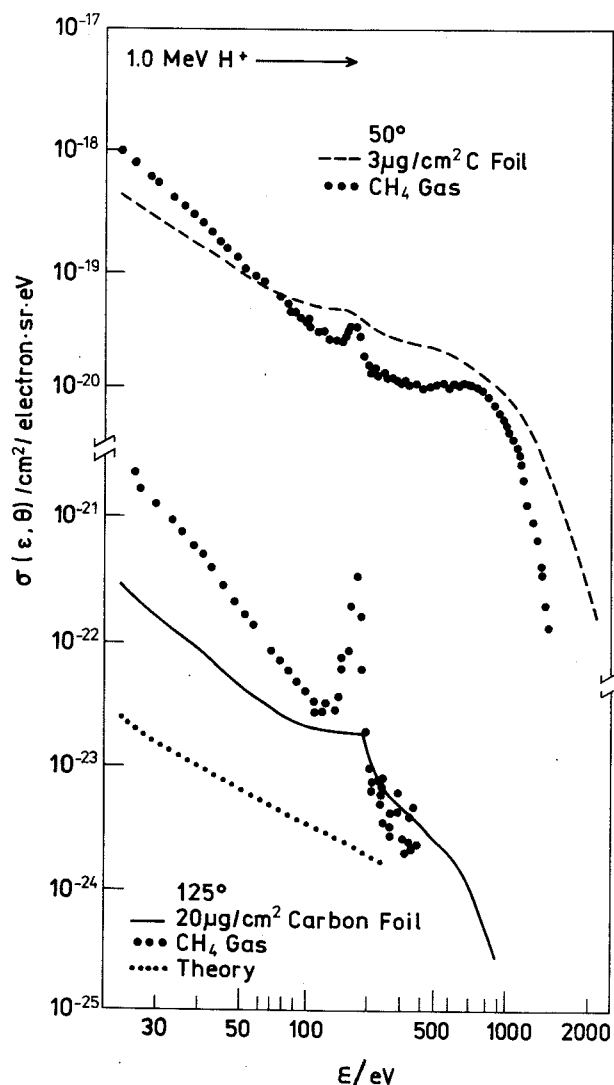


Fig. 5.21. Doubly differential spectra from a carbon foil and an equivalent thickness of methane gas (*i.e.*, the same number of target electrons per unit area) in absolute numbers per target electron, per unit energy, and per unit angle. Theoretical calculation based on Eq. 5.15 from Schou (1980) (from Toburen, 1990).

electrons reduces the number of ionizations at these collisions.

Alkemade *et al.* (1990) measured energy spectra at a fixed exit angle from an aluminum crystal under UHV conditions. These measurements included spectra induced by channeled ions as well.

5.10 Heavy Ions: External Spectra

The energy spectra produced by singly charged heavy ions are similar in many respects to those induced by light ions (Hasselkamp, 1985; 1991; Hofer, 1990). At low ejection energies, the shape is also sensitive to contaminants as described in Sections 5.6 and 5.7. The spectra taken with keV ions show the broadening of the low energy peak compared with incident protons and the increasing full width at half maximum with energy observed in the accessible

range of data up to 1 MeV (Hasselkamp, 1991). The angular distribution of the low-energy electron yield induced by 40-keV Ar⁺ ions was found to be approximated well by a cosine function (Mischler *et al.*, 1984).

At speeds below the Bohr speed v_0 , the liberation of electrons takes place via electron promotion processes (see Section 4.2.3) in solids as well as in gases. The incident heavy atom and a target atom form a temporary molecule, which eventually may lead to electron ejection from one or more highly excited states. In principle, this process is analogous to that in the gas phase described in Section 4, but the single-electron excitations from the conduction band make the analysis fairly complex (Sroubek and Falcone, 1993). These authors calculated the internal spectrum for aluminum ions incident on aluminum.

Energy spectra and electron emission induced by fast heavy ions have been reviewed by Rothard (1995). Multicharged ions above 100 MeV were studied by Schiwietz *et al.* (1990) and Schiwietz (1993). Typically, electrons ejected from carbon foils were detected up to several keV for a variety of ejection angles. The primary particles were partially stripped Ne and U ions incident on foils of thicknesses from 20 to 100 $\mu\text{g}/\text{cm}^2$. Examples of the experimental results are shown in Figure 5.22. The spectra exhibit the same structures as those in Figures 5.5 and 5.21 and

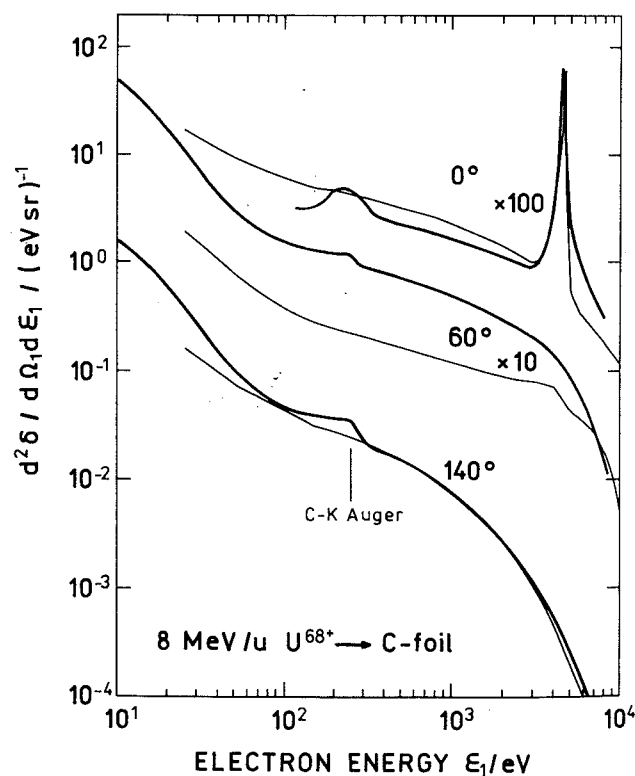


Fig. 5.22. Doubly differential spectra for three different exit angles with respect to the beam direction from a 44 $\mu\text{g}/\text{cm}^2$ thick carbon foil induced by 8-MeV/u U⁶⁸⁺ ions at perpendicular incidence. Solid lines, calculations (from Schiwietz, 1993).

in the gas phase (Section 4). In the forward direction, there is a pronounced peak of convoy electrons. In the other directions, the differential yield from the low-energy peak decreases approximately as ϵ_1^{-2} below the Auger peak around 270 eV. At even higher energies there is a shoulder from binary encounter collisions. Above the shoulder, the intensity falls off precipitously.

The spectra have been described by a transport model developed by Schiwietz *et al.* (1988; 1990) and Schiwietz (1993). In the description, the energy loss and angular scattering were separated. The production of free target electrons was modeled by semi-empirical atomic cross sections and the transport to the surface by the separation procedure. Also, the shift of energy levels and plasmon excitation were incorporated in the model. The theoretical results agree well with the experimental data for backward directions and energies above 4 keV. For slow elec-

trons ejected at large forward angles, there are discrepancies between experimental and theoretical results that exceed a factor of six. These discrepancies can be traced to the neglect of those trajectories that are parallel to the surface.

The total yield from both sides of the foil is about 2500 electrons/ion at these high energies (> 4 MeV/u). The forward ejection yield exceeds the backward yield by more than a factor of two and approximately one-third of the electrons have energies above 100 eV. This contrasts with the symmetric case, which has been studied at lower energies (1 MeV/u) by Rothard *et al.* (1992) and Hasselkamp (1991). At these energies, the low-energy peak is dominant.

Recently, heavy cluster ions have been utilized to study secondary electron production from clean surfaces. These studies include total yields and emission statistics, but no spectra are available (Töglhofer *et al.*, 1993a; 1993b).

6. Applications of Ionization Data to Issues in Radiological Sciences

6.1 Introduction

The spatial pattern of energy deposition in a medium by ionizing radiation has come to be associated with the "tracks" produced by the charged particles as they slow down through subsequent interactions with the medium. With the slowing down of fast charged particles, tracks can be very distinct and may include, along their path, shorter tracks and clusters of ionization produced by the higher energy electrons ejected in small-impact-parameter collisions with the bound electrons in the medium.

Methods for describing the tracks produced by ionizing radiation have evolved from the use of average quantities such as stopping power to the elaborate mathematical models that provide the spatial coordinates of all of the events making up the tracks. The latter cannot be evaluated without a detailed knowledge of the absolute cross sections for the production and subsequent interactions of secondary electrons in ionizing events; these cross sections are needed as a function of the energy and emission angle (*i.e.*, the DDCSs described in Section 1.2) of both the primary projectile and secondary electrons in order to determine the spatial coordinates of all the energy loss events. The DDCSs for emission of electrons in ionizing collisions also provide insight into some of the quantities commonly used in radiological physics, *e.g.*, stopping power and *W*-values (the *W*-value is the average energy required to produce an ion pair, see ICRU, 1979).

It is instructive to look closely at a simulated charged-particle track and discuss some of the parameters that have been used in the literature to describe the characteristics of energy deposition along its path. The illustration in Figure 6.1, originally presented by Goodhead (1987), provides a description of the track features commonly used in radiation research. In this example, a Monte Carlo simulation of an 8-MeV alpha particle passing through water vapor is used to determine the spatial coordinates of the ionization produced along a segment of the alpha particle's path; all dimensions are scaled to represent material of unit density (1 g/cm³; that of liquid water), to illustrate the extent of charged particle transport in a biologically relevant medium. It must be noted that track structure features are stochastic quantities, therefore one should not expect all of the features shown in Figure 6.1 to be routinely observed in such a short section of the particle path. Rather, this track segment was judiciously chosen from a catalog of track segment simulations for illustrative purposes. When general conclusions are derived from such simulations, proper averages over independent track segments must be employed.

The development of stochastic descriptions of the energy deposition process has been explored in several ways, *e.g.*, by means of computational track structure simulation as shown in Figure 6.1 and through the use of proportional counter techniques (Rossi, 1968; ICRU, 1983; Rossi and Zaider, 1995). These techniques allow one to obtain distributions of energy deposited in small simulated "tissue-like" volumes. The dashed circle superimposed on the particle track in Figure 6.1 represents the cross sectional area of a spherical or cylindrical counter in which the energy deposited by the particle is measured. This technique provides information on the stochastics of energy deposition in terms of the two principal quantities of microdosimetry. The *specific energy*, which is the stochastic analog of absorbed dose, is defined as the energy absorbed per unit mass in a specified volume. The *lineal energy* is the energy absorbed in a specified volume divided by its mean chord length. It differs from the non-stochastic quantities, stopping power and LET, in that it is restricted to energy deposited within a geometrically defined volume. Of particular significance to radiation biology has been the use of microdosimetric event size distributions, in either lineal energy or specific energy, to better understand the biological effectiveness of mixed radiation fields.

Grid-walled, or "wall-less," proportional counters have also been used in association with coincidence circuitry to measure the distributions of energy deposited by single ionization events. By the use of a coincidence signal between an energy deposition event and that of a particle detector which defines the position of a fast ion relative to the proportional counter volume, one can gain information on the distribution of energy deposition as a function of the position of the fast particle moving either through or near the volume of the proportional counter. Such information provides a measure of the contribution of secondary electrons to the energy deposited in a small simulated tissue volume. In other words, such measurements help one to evaluate the effects of transport of electrons that are produced by fast ions and that have significant ranges in tissues.

The primary limitation of proportional counter techniques for use in microdosimetry has traditionally been that the minimum size of the volumes that can be reliably simulated by the detector geometry is usually of the order of a few hundred nanometers or larger (Rossi and Zaider, 1995). Such volumes are considerably larger than the dashed circle shown in Figure 6.1, with diameter of about 0.06 μm (60 nm), and detector diameters that simulate volumes with dimensions of about 1 μm are commonly used in practice. Thus, proportional counter techniques actu-

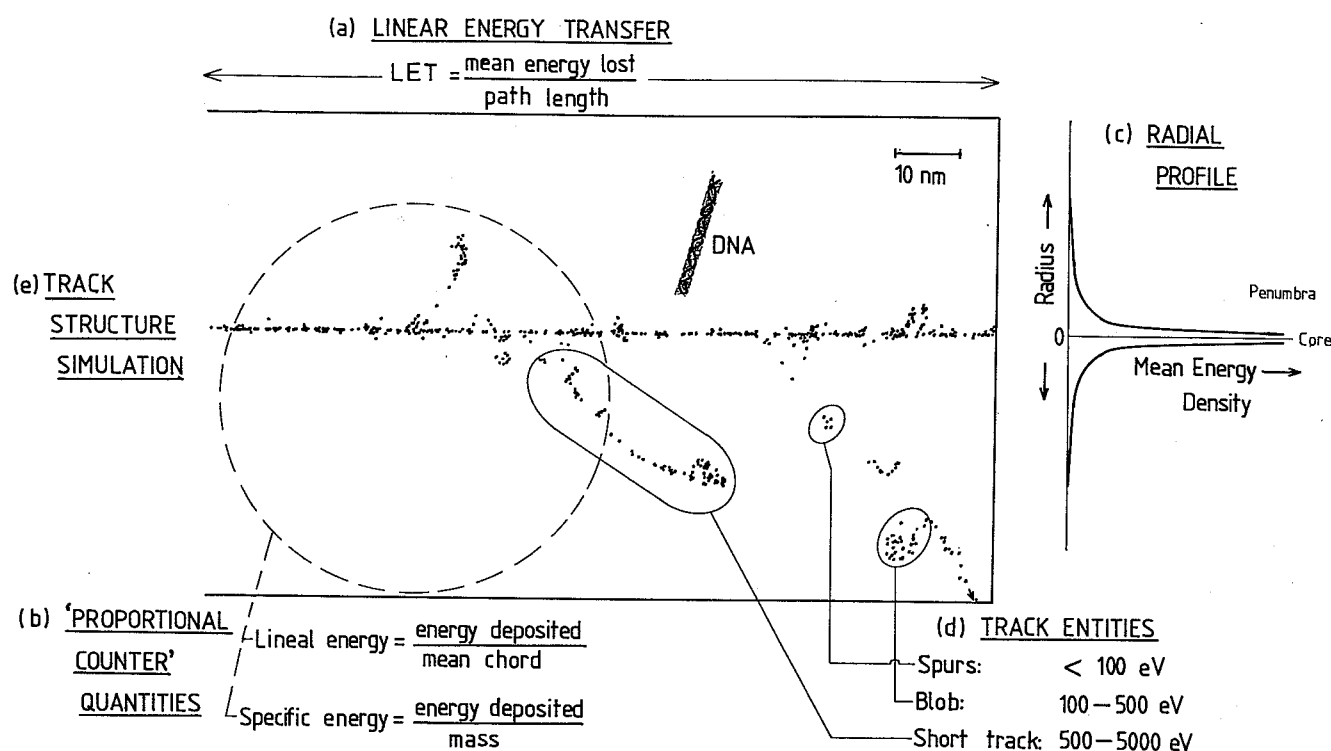


Fig. 6.1. Description of the parameters commonly used to define charged particle track features (after Goodhead, 1987).

ally average over many stochastic features of particle tracks and simulate sizes representative of the larger features of the mammalian cell structures, *e.g.*, the cell nucleus. However, more recently, measurements for simulated sites of diameters of 10 nm have been reported (Kliauga, 1994).

Many studies have been carried out on the determination of the energy deposited in cellular and sub-cellular volumes in the vicinity of tracks, *i.e.*, the energy deposited as a function of distance from the particle trajectory. These studies involved theoretical approaches (Holley *et al.*, 1990; Waligorski *et al.*, 1986; Chatterjee and Shaefer, 1976; Butts and Katz, 1967; Katz, 1970; Katz and Kobetich, 1970) as well as measurements (Varma *et al.*, 1978; Varma *et al.*, 1975; Baum *et al.*, 1974; Baum, *et al.* 1974; Mills and Rossi, 1980). In essence, these radial distributions of energy deposition are an extension of the concept of energy-restricted LET. The radial distribution of energy deposited along the charged particle track is illustrated as part (c), to the right side of Figure 6.1.

Measurements employing proportional counters have also been used to define the radial distributions of energy deposition (Gross, *et al.*, 1969; Glass and Roesch, 1972; Varma *et al.*, 1978; Metting *et al.*, 1988; Toburen *et al.*, 1990a). These measurements have the capability of providing stochastic distributions of energy deposition in small volumes near, or within, the particle's path as well as contributing information on the radial profile of energy deposition perpendicular to the path. Such measurements yield the distribution of actual energy deposition that is usu-

ally zero but can exceed the absorbed dose by several factors of ten.

The type and yields of chemical reactions that follow energy deposition by ionizing radiation are known to depend on the local density of ionization and excitation. Radiation chemists (Samuel and Magee, 1953) traditionally have used track entities they describe as spurs, blobs, and short tracks, to qualitatively distinguish between the different initial conditions presented by absorption of differing amounts of energy from a radiation field (see Section 6.4.1).

6.2 Charged Particle Track Simulation

As studies of radiation biology focus increasingly on the molecular aspects of damage and repair to DNA, it becomes important to better understand the energy deposition in volumes comparable to the dimensions of DNA (Varma and Chatterjee, 1994). A complete description of energy deposition in such small volumes is obtained from Monte Carlo simulation of the charged-particle tracks. For determining the 3-dimensional structure of energy deposition by Monte Carlo techniques, the collision cross sections used in the simulation for ionization must be differential in both the ejected electron energy and emission angle. For calculations involving the stopping of heavy charged particles, cross sections are required for the full energy range of the primary heavy ion and for the full range of secondary electron energies. The range of data needed for Monte Carlo charged particle track simulation represents a large amount of knowledge

and, of course, not all the data exists for the systems of interest in radiation biology. In particular, there are few data available for real biological media, *i.e.*, heterogeneous condensed macromolecules, DNA, proteins, *etc.*, in water.

The extensive database available for DDCSs, *e.g.*, the electron energy spectra measured or calculated as a function of the emission angle, can also be useful in deriving both singly differential and TICSs for use in charged-particle track structure calculations. It should be noted, however, that measured DDCSs are inherently less accurate than measured TICSs, and when available, independently derived TICSs are preferable for use in track structure calculations. Where necessary, however, the differential cross sections can readily be integrated to provide needed integral cross sections. For example, the SDCSs, $\sigma(\epsilon)$, appropriate for the study of energy loss, can be obtained from the DDCSs, $\sigma(\epsilon, \theta)$, by integrating as indicated by Eq. 1.5 and the TICS, σ_i , (this is the cross section for electron production, as contrasted to the counting or ion production cross section described in Section 1.2) can be found from the SDCSs using Eq. 1.7. In addition, one can obtain the mean energy of electrons ejected in ionizing collisions from the definition

$$\bar{\epsilon} = \frac{\int_0^{\epsilon_{\max}} \epsilon \sigma(\epsilon) d\epsilon}{\int_0^{\epsilon_{\max}} \sigma(\epsilon) d\epsilon}, \quad (6.1)$$

and the median energy of the ejected electrons from the equation

$$\int_0^{\epsilon_{\text{median}}} \epsilon \sigma(\epsilon) d\epsilon = \frac{1}{2} \int_0^{\epsilon_{\max}} \epsilon \sigma(\epsilon) d\epsilon. \quad (6.2)$$

The utility and power of the Monte Carlo method for simulating the tracks of charged particles to gain insight into the relative spatial characteristics of different radiations is demonstrated in Figure 6.2, where simulated distributions of energy deposition events are shown for a fast proton track and for electrons emitted in the decay of the radionuclide ^{125}I . The structures shown in Figure 6.2 illustrate, with a 2-dimensional projection of the 3-dimensional structures, the positions of all ionizations, excitations, and "stopped" secondary electrons produced in a simulated tissue following the passage of a 1-MeV proton and, for comparison, similar distributions produced following the Auger-electron cascades initiated by the decay of ^{125}I . These simulated distributions were produced from the Wilson-Paretzke code (MOCA16, Wilson *et al.*, 1988).

The event-distribution of electrons simulated for the decay of ^{125}I was performed using the same Monte Carlo code for the transport of secondary electrons; however, in this case, the initial electron source was provided by the Auger electrons emitted during atomic

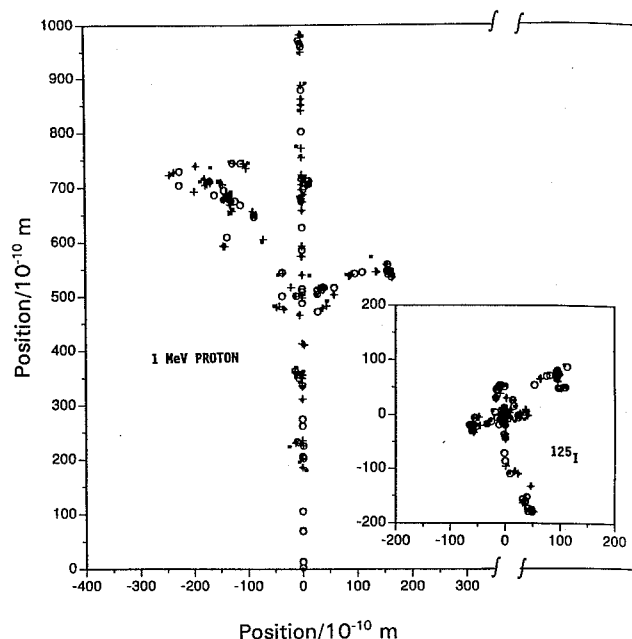


Fig. 6.2. Monte-Carlo simulation of the spatial pattern of excitation, ionization, and subionization electrons produced along the track of a 1 MeV proton and in the Auger cascades following decay of ^{125}I . +, ionizations; O, excitations; ■, subionizations (Subionization electrons are those with energies too low to cause ionization of the medium.) The proton travels from the bottom to the top of the figure. Simulations are from Wilson (private communication) using the techniques described by Wilson *et al.*, 1988).

relaxation following the electron capture decay of ^{125}I (Charlton and Booz, 1981).

An analysis of the features of the energy deposition distributions shown in Figure 6.2 supports our understanding of the relevance of the density of energy deposition on the subsequent biological effectiveness of different types of radiation. The proton track illustrates the relative frequency of ionization to be expected along the path of a "high"-LET charged particle, which may be a recoiling proton generated by neutrons of comparable energy. The particular proton track segment shown in Figure 6.2 illustrates several features of the patterns of energy deposition by ionizing radiation. It contains a fast secondary electron ejected from the inner shell of the oxygen constituent of the simulated medium (the δ -ray to the left of the path of the proton) and an Auger electron (the shorter electron track to the right of the proton path) that is ejected as that inner-shell vacancy is filled. The various components of the proton track also aid our visualization of the density of energy deposition resulting from the absorption of x rays and beta particles (fast electrons), where similar or higher energy electron tracks are also generated. For example, the characteristics of energy deposition distributions of fast secondary electrons produced by x rays, which distinguish them from those produced by high-LET particles, is that they are produced at more widely separated positions in the absorbing medium.

Note that the Auger cascades following ^{125}I decay, although also composed of relatively fast electrons, contribute to an even more densely ionizing pattern of energy deposition than that produced by the proton track.

The potential relevance of the relative size of the component features of charged-particle induced track structures is perhaps best illustrated by comparison to the size of DNA features. This comparison is made in Figure 6.3, where a simulated 1-MeV proton track is shown on the same scale as the double helix of DNA, which is depicted in the linker region and wrapped around nucleosomes, which, in turn, are aggregated in a condensed 30 nm diameter DNA fiber. The denser spatial pattern of energy absorption of high-LET radiation usually results in enhanced effectiveness for DNA damage such as double strand breaks. This is one of the causes of the elevated RBE for cellular damage. An additional one has been attributed to differences of energy concentration at the micrometer level (Rossi and Zaider, 1992).

The distributions of excitation and ionization for charged particles shown in Figures 6.2 and 6.3 were calculated using the Monte Carlo code of Wilson and Paretzke (Wilson *et al.*, 1988) in which the electron production and transport is based on gas-phase data. This use of gas-phase data, although common (Wilson and Paretzke, 1981; Charlton *et al.*, 1985; Goodhead *et al.*, 1985; Goodhead and Brenner, 1982; Michalik, 1993; Kraft *et al.*, 1992), is often questioned because

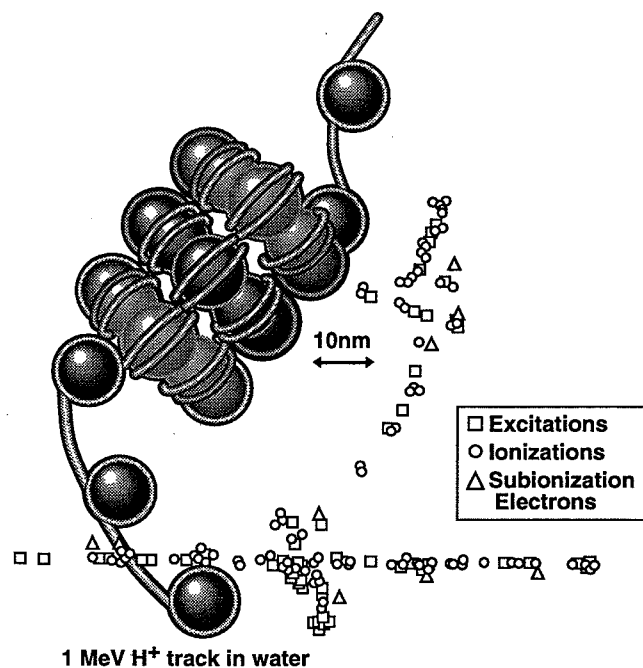


Fig. 6.3. Spatial pattern of excitation, ionization, and subionization electrons compared to the dimensions of DNA structures including the double helix (linker region), DNA wrapped around nucleosomes and a section of condensed 30 nm DNA fiber. Simulations are from Wilson (private communication) using the techniques described by Wilson *et al.* (1988).

the biological medium is a heterogeneous condensed-phase material. It is used, however, because it is the only data available for which one has experimental tests of the cross sections and interaction models used and because the effects of phase are expected to be small relative to uncertainties in the knowledge of condensed-phase cross sections. It is well documented that molecular binding affects the electron spectra of ejected electrons only below about 30 eV (Toburen, 1991), and since the energy associated with the change in phase is considerably smaller than the molecular binding energy, the change of phase may be expected to affect energy loss events at even smaller energies. Thus, phase effects should influence only a very small portion of the ejected electron spectra. In addition, cross sections for condensed-phase material, such as water, are available only by theoretical techniques (see Wright *et al.*, 1985 and references therein; Kaplan *et al.*, 1986; Zaider, 1991) and they have not, for the most part, been tested against measured quantities. Those track simulation models that incorporate condensed-phase cross sections often must incorporate gas-phase data in other areas, such as branching ratios for dissociative ionization and elastic scattering of low-energy electrons, which also detracts from their ability to produce tracks that have truly liquid phase characteristics.

The primary differences between the physics of energy deposition in the condensed phase and that in the gas phase are generally considered to be in the oscillator strength and in the delocalization of the energy deposition due to the collective motion of the target electrons. In a gas atom or molecule, the target, electron is more localized than in a solid where the electronic wave functions of the target electrons may spread over a relatively large distance making it inappropriate to specify the precise coordinates of the energy loss event (Zaider, 1991).

The implications of the phase of the stopping medium on energy deposition has been discussed by Inokuti (1991). One can explore the implications of these effects on electron transport, an important factor in track structure, and more importantly on the subsequent chemical and biological processes, by direct comparison of quantities calculated with the different codes. Paretzke *et al.* (1991) presented a comparison of the spatial distributions of energy deposition and ionization, as simulated by vapor phase (Paretzke, 1987) and liquid phase Monte Carlo codes (Hamm *et al.*, 1985). The primary difference in the underlying physics used in these two codes, other than the use of appropriate oscillator strength distributions for liquid versus gas phase interactions, is that in the liquid, energy may be deposited to quantized collective states (plasmons) which, according to the authors, may involve the coherent contributions of as many as 10^9 electrons. These collective states are postulated to account for the large peak in the